

# Decoupling between Shockley partials and stacking faults strengthens multiprincipal element alloys

Zongrui Pei<sup>a,1</sup>, Siyuan Zhang<sup>b</sup>, Yinkai Lei<sup>c</sup>, Fan Zhang<sup>d</sup>, and Mingwei Chen<sup>e,f</sup>

<sup>a</sup>Oak Ridge National Laboratory, Oak Ridge, TN 37831; <sup>b</sup>Max-Planck-Institut für Eisenforschung GmbH, D-40237 Düsseldorf, Germany; <sup>c</sup>Department of Mechanical Engineering and Materials Science, University of Pittsburgh, Pittsburgh, PA 15260; <sup>d</sup>WPI Advanced Institute for Materials Research, Tohoku University, Sendai 980-8577, Japan; <sup>e</sup>Department of Materials Science and Engineering, Johns Hopkins University, Baltimore, MD 21218; and <sup>f</sup>Hopkins Extreme Materials Institute, Johns Hopkins University, Baltimore, MD 21218

## Abstract:

Mechanical properties are fundamental to structural materials, where dislocations play a decisive role in describing their mechanical behavior. Although the high-yield stresses of multiprincipal element alloys (MPEAs) have received extensive attention in the last decade, the relation between their mechanistic origins remains elusive. Our multiscale study of density functional theory, atomistic simulations, and high-resolution microscopy shows that the excellent mechanical properties of MPEAs have diverse origins. The strengthening effects through Shockley partials and stacking faults can be decoupled in MPEAs, breaking the conventional wisdom that low stacking fault energies are coupled with wide partial dislocations. This study clarifies the mechanistic origins for the strengthening effects, laying the foundation for physics-informed predictive models for materials design.

## Keywords:

Multiprincipal Element Alloys; Strengthening Mechanism; Stacking Faultenergy; Dislocation

## Acknowledgement:

This work was sponsored by the US Department of Energy, Office of Science, Basic Energy Sciences, Materials Science and Engineering Division. This research used resources of the Oak Ridge Leadership Computing Facility, which is supported by the Office of Science of the US Department of Energy Contract DE-AC05-00OR22725. M.C. was supported by NSF Grant DMR-1804320

Multiprincipal element alloys (MPEAs) have triggered ever-increasing interest from the physics and materials science community due to their huge unexplored compositional space and superior physical, mechanical, and functional properties (1–12). They also provide an ideal platform to study fundamental physical mechanisms (6, 9, 13, 14). With the rise of MPEAs, understanding their mechanical properties has become a central topic in materials science in the last decade. In face-centered cubic (fcc) MPEAs, the motion of partial dislocations (Shockley partials) and their associated stacking faults (SF) defines their mechanical properties. Alloys with low SF energies (SFEs) have more extended SFs, which are generally believed to have more strength and ductility through twinning-induced plasticity (TWIP) and transformation-induced plasticity (TRIP) mechanisms (15–17).

Although extensive endeavors have been made, the commonalities in the origins of high-yield stresses shared by many MPEAs remain elusive. Among the most common intrinsic contributions of yield stresses are the lattice friction (or Peierls stress) and solute solution strengthening (18–22). Since the birth of MPEAs, it has been a controversy about the relative importance of Peierls stress among the other contributions of yield stress, including the solid-solution strengthening effect (18, 21–23). Many researchers assume small Peierls stresses based on the common wisdom of conventional alloys and pure metals (24, 25) and the low SFEs in MPEAs. Low SFEs usually accompany small Peierls stresses. Overall, this controversy originates from the lack of accurate dislocation geometry in MPEAs, which allows for a direct, critical evaluation of the Peierls stress. There are reports on the dislocation geometry in MPEAs, but almost all of them focused on the widths of SFs (26–28). In contrast, the core widths of Shockley partials are rarely reported for MPEAs, partly due to the difficulty in measurements and partly due to unawareness of its importance. To address this issue, we need very accurate determination of the core width of the Shockley partials. It is an important input parameter for mechanical simulations and various theories and models (21, 29–31). Here, we adopt three of the most extensively studied MPEAs, NiCoCr, VCoNi, and CoCrFeNiMn, and their only common fcc element, Ni, to address the above issues.

The commonalities in the origins of high-yield stresses shared by the MPEAs can be indicated by the minimum energy profile along the dislocation motion path, i.e., the increased energies introduced by generalized SFEs (GSFEs; Fig. 1A). The local minima of the curves are SFEs, and the maxima are the theoretical energy barriers for pure shearing, which is a good indicator of the changes of Peierls stresses. Assisted by the accurate density functional theory (DFT), we compute GSFE curves for several representative MPEAs and their common fcc component Ni. This identifies a surprising fact: One of the representative MPEAs, NiCoCr, has a decoupled strengthening effect, i.e., it has a narrower dislocation core of Shockley partial than pure Ni, although its SF is much wider than Ni. Usually, in fcc alloys, when SFE is lower, its unstable SFE (USFE) (maximal GSFE) is also lower, which is coupled. Examples include the two other MPEAs, VCoNi and CoCrFeNiMn, and many Mg alloys (basal plane dislocations) (25) and Al alloys (32). However, NiCoCr does not follow this convention. The understanding from multiscale simulations, atomistic simulations, and the high-angle annular dark-field scanning transmission electron microscopy (HAADF-STEM) images rationalizes the narrow core of Shockley partials. These results clearly reveal the diverse and decoupled mechanistic origins for the strengthening effects in the MPEAs with excellent mechanical properties.

## Decoupling Mechanistic Origins Revealed by GSFEs

GSFE is a very useful tool to gain insight into the different mechanisms of deformation. For example, the USFE ( $\gamma_u$ ) indicates the contribution of Peierls stress; the magnitude of SFE offers information on the TRIP and TWIP deformation mechanism (16). Supercells of 72 atoms ( $4(1/2[110]) \times 3(1/2[1\bar{1}2]) \times 6(1/3[1\bar{1}\bar{1}])$ ) are employed to calculate GSFEs for Ni, VCoNi, NiCoCr, and CoCrFeNiMn. Increasing the faulted planes from 6 to 12 only gives negligible changes of SFEs (-0.030 to -0.033 Jm<sup>-2</sup> for NiCoCr). Atoms are randomly placed on the lattice sites in the supercells for various configurations, and the number of configurations considered is determined by convergence tests (33) (e.g., SI Appendix, Fig. S1). We calculate the GSFEs for three representative alloys with excellent mechanical properties and use their common fcc component Ni as a reference.

The GSFE curves of Ni, NiCoCr, VCoNi, and CoCrFeNiMn (the Cantor alloy) are shown in Fig. 1 with key points listed in Table 1. It is worth mentioning that the curves in Fig. 1C are the GSFEs along the white arrows ( $1/6[112]$ ) rather than the orange arrow ( $1/2[110]$ ) in Fig. 1D. The reason for the negative SFEs is that these alloys are metastable in the fcc structure and have lower energies in the hexagonal close-packed structure (hcp) than in fcc. The so-called Axial-Next-Nearest-Neighbor-Ising model suggests that SFE is proportional to the energy difference between the two close-packed structures (34–37). The common feature of all three alloys is that their lower SFEs help activate the various deformation modes facilitated by partial dislocations, such as the TRIP mechanism. One surprising finding is that NiCoCr has a much lower SFE than Ni; its energy barrier USFE is, however,

obviously higher than Ni. Given the inverse relationship between SFE  $\gamma_0$  and SF width  $x_0 = \frac{\mu \bar{b}}{\gamma_0} \frac{b}{24\pi} \frac{2+\nu}{1-\nu}$  (Burgers vector  $\bar{b}$  shear modulus  $\mu$ , and Poisson ratio  $\nu$ ), we find narrower SF width than NiCoCr. Here, the SFE at room temperature for NiCoCr is adopted, e.g., 0.022 Jm<sup>-2</sup> (38). For a perfect dislocation when its restoring force takes a simple sinusoidal shape, its half-width, i.e., the core width at the half height of its misfit-function peak, can be approximated by  $w \approx Kb^2/4\pi\gamma_u$  (29).  $K = \mu/(1 - \nu)$  is an elastic constant for edge dislocation. This indicates that the larger energy barrier of NiCoCr may give a smaller half-width. However, this needs to be further confirmed by more accurate methods, since the formula for perfect dislocation may fail for dissociated dislocations.

The GSFEs of NiCoCr indicate the exceptional decoupling in the variation of dislocation geometry, i.e., SF widths and the half-widths of Shockley partials can change in opposite directions, providing another pathway to tune mechanical properties. It is widely acknowledged that low SFE promotes the activation of the TWIP and TRIP mechanisms, making the alloy more ductile

and stronger. The same origin applies to VCoNi and CoCrFeNiMn. In contrast to VCoNi and CoCrFeNiMn, NiCoCr is unique since its SFE is lower than pure Ni, but the USFE is higher than Ni, demonstrating that its excellent mechanical properties have an additional origin, i.e., the increased Peierls stress. The decoupled strengthening mechanisms in NiCoCr show that the high-yield stresses in MPEAs have diverse origins.

### Consequences of Decoupled Mechanisms Confirmed by a Revised Peierls-Nabarro Model

We move forward to further check if the half-width  $w$  of the Shockley partial in NiCoCr is indeed smaller than in pure Ni by modeling its geometry directly. This is one of the consequences of the increased USFE in NiCoCr. DFT is accurate to describe dislocation geometry (39, 40). However, it is infeasible to describe MPEAs, given that MPEAs require a much larger supercell and longer relaxation time for each ionic step. Moreover, the random feature of MPEAs requires multiple calculations to sample over different atomic configurations for the same geometry, since only statistic geometry is practically meaningful. Specifically, NiCoCr is more stable in hcp structure than in fcc at 0 K, which also makes direct DFT calculations of random alloys impractical. Fortunately, the Peierls–Nabarro model and its many revised versions (25, 41–45) offer a more convenient method to inspect the dislocation geometry in Ni and NiCoCr.

One of the key input parameters for the revised Peierls–Nabarro model (45) is the gamma surface  $\gamma$  (Fig. 1). The elastic constants and Burgers vectors for NiCoCr and CoCrFeNiMn are adopted from the seminal paper of Varvenne et al. (21) We obtained these parameters from our DFT calculations for VCoNi, i.e.,  $G = 77.7$  GPa,  $b = 2.53$  Å; the Poisson ratio  $\nu$  is taken as 0.33, which is an average of their experimental values. The so-called multiple-equal-fractional-dislocation (MEFD) formulation (45) introduces one extra freedom to the original Peierls–Nabarro model, which is particularly useful for the compact dislocation core. The calculated dislocation cores for NiCoCr and pure Ni are shown in Fig. 2. The SF width of NiCoCr is theoretically infinite, which is a direct consequence of its negative SFE. However, the SF width cannot be actually infinite in a literally finite-size sample in experiment. They are demonstrated by very wide SFs profuse under high-resolution microscopy (27, 35, 46). In contrast, the SF width of Ni is finite, which is about 5.5 times the Burgers vector. The half-width of a Shockley partial in Ni is  $0.70b$ , while that in NiCoCr is  $0.56b$ , with a ratio of 1.25 (see Table 2). At room temperature, negative SFEs can become positive (35, 47, 48), e.g.,  $0.022$  Jm<sup>-2</sup> for NiCoCr (38). Adoption of this room-temperature SFE in our model yields only a slight change of half-width from  $0.56b$  to  $0.62b$ , which is unambiguously smaller than  $0.70b$  (0 K) or  $0.72b$  (room temperature) of pure Ni. This confirms the wider core of Ni than NiCoCr that is indicated by their USFEs  $\gamma_u$ . These results are listed in Table 1.

In addition to the GSFE method and DFT-informed Peierls–Nabarro modeling, we also adopt a modified embedded-atom method (MEAM) potential (49) to perform molecular statics calculations (50) for the same dislocations in NiCoCr and Ni. The displacement fields for the two systems are directly extracted from the relaxed atomistic structures and are shown in *SI Appendix*, Fig. S2. The displacement fields are then fitted to a Lorentzian peak  $\rho(x; w) = w/(x^2 + w^2)$ , which yields the half-width  $w$  for Shockley partials. The  $w$  of Ni is also wider than NiCoCr, with a ratio of  $w(\text{Ni})/w(\text{NiCoCr}) = 1.15$ . This is consistent with the above results.

### Direct Measurement of the Half-Width of Shockley Partial by HAADF-STEM

The half-width of the dislocation core is one of the key parameters that determine Peierls stress. Although the theoretical methods can reliably confirm the  $w$  in Ni is wider than that in NiCoCr (25), the accurate half-width needs to be calculated from experimental measurements, since Peierls stress is sensitive to its magnitude (45). Some researchers measured dislocation geometry, but mainly the width of SFs (27, 28, 40). Few people measure the half-width of Shockley partials in pure Ni, which is not easy because of the interference of its narrow SFs. Fortunately, the SFs of MPEAs are multiple times wider than Ni, and the interference can be negligibly small. Here, we will adopt the state-of-the-art processing techniques for HAADF-STEM images to accurately measure the core width of the Shockley partial in one representative MPEA, i.e., NiCoCr.

The profuse Shockley partials in deformed NiCoCr are taken by HAADF-STEM for a statistical analysis (Fig. 3A). We use several of the latest processing methods to extract the atomic positions from HAADF-STEM (Fig. 3). It treats each bright atomic position as a two-dimensional (2D) distribution of the pixels (of the order of 100). The intensity is fitted to a 2D Gaussian function of a bell shape, i.e.,  $f(x, y) = A \exp\left(-\frac{(x-x_0)^2}{2a^2} - \frac{(y-y_0)^2}{2b^2}\right)$ . Here,  $A$  is a prefactor, and  $a, b$  are the variances along the two principal axes (Fig. 3B). The mean  $(x_0, y_0)$  of the Gaussian function  $f(x, y)$  is considered as the position of that atom. Local distortion can be corrected or even removed by considering the nearest neighbors of the atom during the extraction process. This method is numerically accurate, repeatable, and independent of researchers' experience. If the atoms are not in a line parallel to the horizontal direction, but with an angle of  $\theta$ , a correction of  $1/\cos(\theta)$  is needed for the interatomic distances. The interatomic distances are rescaled by the average distance between atoms in the reference (defect-free) region. This can correct the inclination of the projection plane. See *SI Appendix* for more details.

We analyze seven high-quality HAADF-STEM images with the above procedure to extract all relevant atomic positions. As is shown in Fig. 3C, we use arc-tangent function  $u(x; w) = b/2\pi \arctan(x/w) + b/4$  to fit the HAADF-STEM atomic positions, which shows all the atomic positions approximately falling on the curve. The fitting yields a half-width for NiCoCr with an average of  $1.23b \pm 0.44b$ . This is narrower than common pure metals with a range of  $1.61b \sim 1.81b$  after considering a small correction factor (*SI Appendix*) (23, 51).

The fact that NiCoCr has a relative narrow core of Shockley partial is one of the important origins for its high-yield stress. The

small  $w$  can impact yield stress through both solid-solution strengthening and Peierls stress. The former can be deduced from the Varvenne model (21). It predicts a higher-yield stress for a narrow core of Shockley partials. The higher Peierls stress will be demonstrated in the following section.

## Direct Evaluation of Peierls Stress

Peierls stresses can be calculated by using an analytical formula (29) or the Peierls–Nabarro models once the dislocation half-width  $w$  is known. Peierls stress is very sensitive to the magnitude of half-width, i.e., small variance in  $w$  results in substantial change of  $\tau_p$ . The errors from the input parameters can be substantially mitigated by accurate techniques, such as accurate DFT calculations and reliable experimental measurements of dislocation core width.

In Fig. 4, we show the Peierls stresses calculated at various half-widths  $w$  by the Peierls–Nabarro model with our MEFD formulation. The analytical formula for Peierls stress of undissociated dislocations is  $\tau_p/G = 1/(1-\nu) \exp(-2\pi w/b)$  (29), with a scaling factor of  $2\pi$  between  $\ln(\tau_p/G)$  and half-width  $w/b$ . Obviously our DFT-informed method with a slope larger than  $2\pi$  is less sensitive than the analytical formula. The Peierls stress at the experimental  $w$  for NiCoCr is denoted by dashed lines. As a reference, the Peierls stress of pure Ni at  $1.54b$  (the DFT+PN ratio  $1.25 \times 1.23b$  of NiCoCr measured by experiment) is also calculated. The Peierls stress, of the order of 100 MPa for NiCoCr, is much larger than common fcc metals such as Ni (of the order of several MPa) (24, 25) and cannot be ignored for quantitative accuracy. Its contribution to yield stress can be as large as several hundred megapascals. This numerically confirms one of the decoupled strengthening effects through lattice friction. Although this study focuses on edge dislocations that have lower critical resolved shear stress and thus dominate the yielding behavior, the conclusions hold for screw dislocations as well. The difference between edge and screw dislocation is a scaling factor in  $\tau_p$ .

In summary, we revealed the decoupled mechanistic origins for the excellent mechanical properties in the widely studied alloys. NiCoCr has a unique feature that its yield stress can be attributed to both its high lattice friction (narrow core of Shockley partials) and mechanisms through its low SFE; in contrast, the other representative alloys have smaller lattice friction than pure Ni, and their high-yield stresses cannot be attributed to the lattice friction. This offers direct evidence for decoupled and diverse mechanistic origins for the strengthening effects in complex concentrated alloys. The decoupled strengthening mechanisms revealed here not only demonstrate the unusual flexibility of complex concentrated alloys to tune the mechanical properties, but also provide a pathway to design high-performance alloys.

## Materials and Methods

### *Dislocation Cores Calculated from Experiment*

The Peierls stresses and dislocation cores of common pure metals were systematically studied by Kamimura et al. (51). The Peierls stresses of pure metals are usually of the order of 1 to 10 MPa, which are orders of magnitude smaller than NiCoCr, which offers insights into the deformation mechanisms of MPEAs.

To correctly evaluate the half-width of Shockley partials, several relations between the various quantities are needed. In ref. 51, the values of  $h/b$  are tabulated, which is the distance between slip planes  $h$  divided by the magnitude of Burgers vector  $b$ . The half-width can be obtained by  $w/b = \frac{1}{1-\nu} h/b \approx 1.4h/b \approx 2.0$  when  $\frac{h}{b} = 1.41$ ,  $\nu = 0.3$ . Therefore, for the metals (Cu, Ag, Au, Al, etc.), the half-width  $w$  is about  $2.0b$ . The reference does not include the value for Ni, which was calculated by Zhao and Nieh from experimental data (23). They showed that pure Ni has a core structure of  $1.77b$  comparable to the other metals, but larger than  $1.23b$  of NiCoCr, after considering a small form factor.

One note is needed here. These experimental half-widths are for perfect dislocations, which are slightly different from those of Shockley partials. The difference is approximately controlled by the dislocation character factor  $f = \sin^2(\theta)/(1-\nu) + \cos^2(\theta)$ , where  $\theta$  is the angle between Burgers vector and line direction. For Shockley partial  $\theta = 60^\circ$ ; for perfect dislocation  $\theta = 90^\circ$ . This gives a ratio of  $w(\text{perfect})/w(\text{Shockley}) = f(\text{perfect})/f(\text{Shockley}) = 1.1$  when the Poisson ratio takes 0.3. This is numerically confirmed by the well-known paper of Lu et al. (52), which gives a ratio of 1.16. After including this factor, we can still conclude that pure metals including Ni ( $1.61b$  – e  $1.23b$ ) of NiCoCr.

### *Procedure to Extract Dislocation Displacement Field*

Ingots of the equiatomic NiCoCr were produced by arc-melting from high-purity elemental metals (99.9 wt.%). The melted button was flipped and remelted at least five times and then drop-casted into a rectangular cross-section mold with sizes of 19.4 mm  $\times$  15.8 mm. The cast ingots were then sealed in an evacuated quartz tube and homogenized at 1,473 K for 24 h. The ingots were subsequently cold-rolled along the longitudinal ingot direction to sheets with a final thickness of 9 mm. The rolled sheets were then annealed at 1,173 K for 1 h, followed by water cooling. The sheets were then deformed by shock loading (53). Atomic resolution images of the NiCoCr samples were acquired by using the aberration-corrected JEOLARM-200F STEM operated at 200 kV. Bright-field (BF) and HAADF-STEM images were acquired by using a Gatan BF detector and an annular detector with collection angles ranging from 100 to 267 mrad, respectively. These images were firstly screened for high-quality ones that clearly showed the atomic positions in the dislocation core region. We then used Atomap (54) to extract the atomic coordinates

for further processing to get the dislocation core. The atomic coordinates immediately above the slip plane  $u+(x)$  were subtracted from those below the slip plane  $u-(x)$  to get the displacement field  $u(x) = u+(x) - u-(x)$ ; for those not parallel to the horizontal  $x$  direction and with a misorientation angle  $\theta$ , a correction was made by  $u(x)/\cos(\theta)$ . The key techniques included 1) treating each atom spot as a 2D Gaussian distribution with an elliptical shape and taking the center of the ellipse as the atomic positions; and 2) adjusting the atom positions by considering the positions of neighboring atoms.

### DFT Calculations

Spin-polarized DFT (55, 56) simulations were carried out by using the Vienna Ab Initio Simulation Package (57) to obtain the total energies for the GSFE calculations. The generalized gradient approximation parametrized by Perdew–Burke–Ernzerhof (58) was used to calculate the electronic exchange–correlation interaction, and the Kohn–Sham equation was solved by using the projector-augmented wave method (59), where the Brillouin zone was sampled by using the Monkhorst–Pack scheme (60). The atomic configurations of elements in the pseudopotentials used in our calculations are Co [Ar]3d<sup>8</sup> 4s<sup>1</sup>, Cr [Ar]3d<sup>5</sup> 4s<sup>1</sup>, Ni [Ar]3d<sup>8</sup> 4s<sup>2</sup>, Mn [Ar]3d<sup>6</sup> 4s<sup>1</sup>, Fe[Ar]3d<sup>7</sup> 4s<sup>1</sup>, and V [Ne3s<sup>2</sup>] 3p<sup>6</sup> 3d<sup>4</sup> 4s<sup>1</sup>. Supercells of 72 atoms were employed to calculate GSFEs for Ni, VCoNi, NiCoCr, and CoCrFeNiMn. Once the lattice constants were optimized, only the ionic positions were relaxed in the GSFE calculations; the supercell shape and volume were fixed. This is sufficient since we are interested in the trend of GSFE changes. The relaxation stops when the energy difference between ionic steps is smaller than 10<sup>-4</sup> eV. A plane-wave cutoff of 350 eV and the  $k$ -point meshes of 6×4×4 for Brillouin zone were used. An increase of  $k$ -point meshes by 8 times (2×2×2) the change in total energy is less than 2 meV, or 0.028 meV per atom. Multiple random configurations for the calculations of one GSFE allowed us to evaluate the average and variance of the GSFE.

### Revised Peierls-Nabarro Modeling

The MEFD formulation was used to solve the Peierls–Nabarro equation (45), where for dissociated edge dislocations, the edge and screw components of the trial misfit functions,  $u_e(x)$  and  $u_s(x)$ , are written as

$$u_e(x) = \frac{b}{2\pi} \frac{1}{2N+1} \sum_{i=-N}^N \sum_{j=\pm 1} \arctan\left(\frac{x - jd_0^e - id_1^e}{w_e}\right) + \frac{b}{2}, \quad [1a]$$

$$u_s(x) = \frac{\sqrt{3}b}{6\pi} \frac{1}{2N+1} \sum_{i=-N}^N \sum_{j=\pm 1} j \arctan\left(\frac{x - jd_0^s - id_1^s}{w_s}\right), \quad [1b]$$

where  $N$  is the number of arctangent functions for one partial,  $b$  is the magnitude of the Burgers vector for the perfect dislocation, and  $w$  signifies the half-width of one Lorentzian peak.  $d_0$  is the distance between partials (34, 45). A total of six  $d$ ,  $w$  parameters were optimized for each  $N$  using the Particle Swarm Optimization algorithm (25, 34, 61). Here, we adopted 100 particles and 100,000 steps for each optimization, which gives reliable results. The methods have been implemented in the Dislocation Simulation Toolkit (62). The MEFD formulation has been successfully used to study Mg (45), MPEAs (19), and 2D materials (63).

### Dislocation Cores by Atomistic Simulations

In addition to DFT, multiscale modeling, and experiment, atomistic simulations are also useful to indicate the relative magnitude of core widths of dislocations, although the quality of the results should be taken carefully. The Large-Scale Atomic/Molecular Massively Parallel Simulator (50) was used to optimize the core structure of the dislocations. Here, we adopted one widely acknowledged MEAM potential for such simulation (49). Periodic boundary condition was used in all three axes of the simulation cell. The conjugate gradient method was used to optimize both the atomic positions and the lengths of three cell axes at 0 K and the external pressure of 0 atm. The optimization stopped when the force exerted on all atoms was less than 10<sup>-12</sup> eV/Å. Our simulations used a supercell size of 100([110]) × 5([ $\bar{1}$ 12]) × 10([1 $\bar{1}$ 1]). The perfect edge dislocation on the [1 $\bar{1}$ 1] plane was inserted at the center of the supercell. After relaxations, the atomic positions below and above the slip plane were extracted to calculate the displacement field for the dislocations. The displacement field was fitted to Lorentzian peaks to obtain the half-width of Shockley partials. The procedure is similar to that for the experimental displacement field.

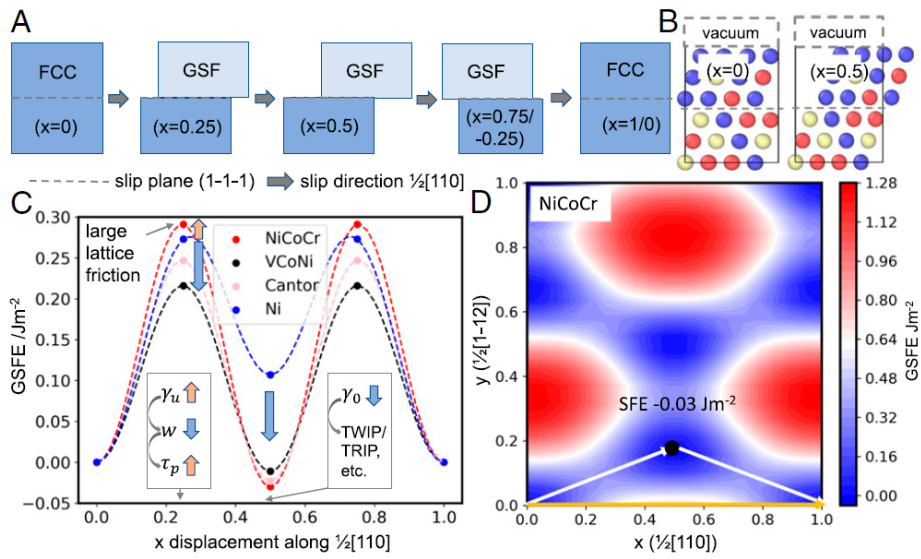


**Fig. 1.** GSFs of three representative MPEAs and pure Ni. (A) The schematic for the generation of GSFs along the slip direction. The displacement 0.75 is equivalent to  $-0.25$  due to the adopted periodic boundary condition. (B) The atom models at two representative displacements for GSFs. (C) The dashed lines are the fitting of the data points to equation  $\gamma = \gamma_0 \sin^2(\pi x) + (\gamma_u - \gamma_0/2) \sin^2(2\pi x)$  (64, 65). (D) The GSFs in C are along the path indicated by the white arrows on the gamma surface, i.e., the minimum energy projected along the path denoted by the orange arrow. The GSF curves reveal the origin for the wide SF and smaller half-width of Shockley partial of NiCoCr than Ni. We need to decrease SFE, while increasing  $\gamma_u$ , in order to optimize the mechanical properties.

**Table 1.** The SFEs and USFEs of Ni, NiCoCr, VCoNi, and CoCrFeNiMn in Jm<sup>-2</sup>

Material	SFE	USFE
Ni	0.107, 0.110 (68), 0.120–0.130 (66)	0.273, 0.273 (68)
NiCoCr	-0.030, -0.026 (69), -0.024 (70)	0.291
VCoNi	-0.011	0.216
Cantor	-0.023, -0.010~ -0.050 (3)	0.247

The SFEs at room temperature for the three MPEAs are described in Table 2.

**Table 2.** Comparison between the dislocation geometry of NiCoCr, VCoNi, CoCrFeNiMn, and Ni

	DFT+PN* (DFT+PN <sup>†</sup> )	EAM
w(Ni)/w(NiCoCr)	1.25 (1.16)	1.15
w(Ni)/w(VCoNi)	0.88 (0.82)	—
w(Ni)/w(Cantor)	1.17 (1.05)	—

NiCoCr has a narrower core of Shockley partial than Ni, which is confirmed by DFT-informed Peierls–Nabarro model (DFT+PN) and EAM simulations.

\*DFT-computed SFEs for the three concentrated alloys.

<sup>†</sup>Positive SFEs at room temperature for the alloys, e.g., 0.022 Jm<sup>-2</sup> for NiCoCr (38),  $\sim 0.030$  Jm<sup>-2</sup> for VCoNi (67), and 0.030 Jm<sup>-2</sup> for the Cantor alloy (26).

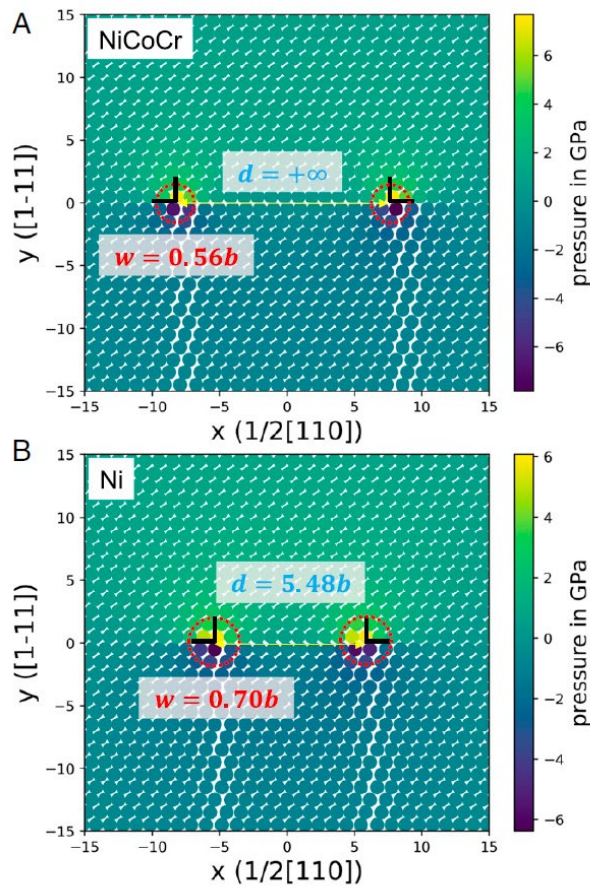


Fig. 2. The dislocation geometry of (A) NiCoCr and (B) Ni. The half-widths for Shockley partials are featured. The dislocation core structures are calculated numerically by a revised Peierls-Nabarro model. Using SFEs at 0 K in the model yields  $0.56b$  for NiCoCr and  $0.70b$  for pure Ni; when SFEs at room temperature are adopted for NiCoCr (38) and Ni (66), the half-widths become  $0.62b$  and  $0.72b$ , respectively.

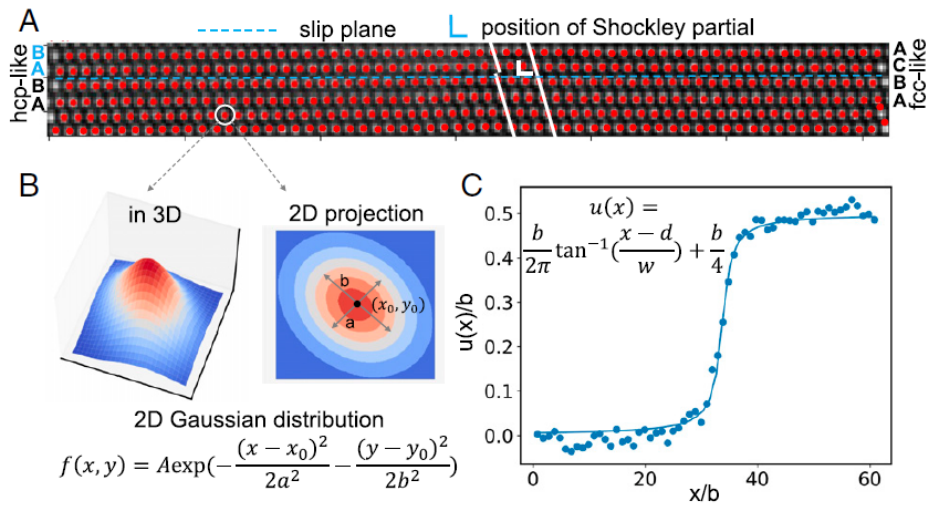


Fig. 3. Direct measurement of dislocation geometry by HAADF-STEM. (A) An example to show the extraction of atomic positions from HAADF-STEM using an accurate method implemented in *Atomap* (51). (B) The 2D Gaussian distribution used to fit the intensity distribution of the pixels around each atom in A. The position  $(x_0, y_0)$  is adjusted according to its neighboring atoms. (C) The displacement field of the Shockley partial in A is fitted to an arc-tangent function to obtain the half-width of Shockley partial.

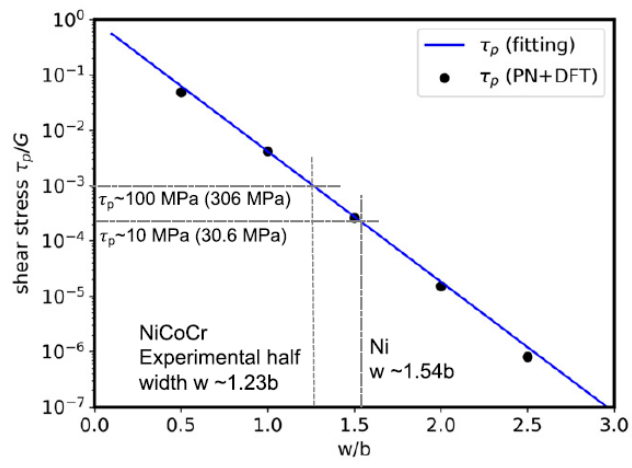


Fig. 4. Evaluations of the Peierls stresses for NiCoCr and Ni. The Peierls stress  $\tau_p$  is determined jointly by experiment and revised Peierls–Nabarro model informed by DFT. The numbers in brackets are the contributions to yield stresses after a Taylor factor of 3.06 is included.

## References

1. J. W. Yeh et al., Nanostructured high-entropy alloys with multiple principal elements: Novel alloy design concepts and outcomes. *Adv. Eng. Mater.* 6, 299–303 (2004).
2. B. Cantor, I. Chang, P. Knight, A. Vincent, Microstructural development in equiatomic multicomponent alloys. *Mater. Sci. Eng. A* 375–377, 213–218 (2004).
3. Y. Zhang et al., Microstructures and properties of high-entropy alloys. *Prog. Mater. Sci.* 61, 1–93 (2014).
4. E. P. George, D. Raabe, R. O. Ritchie, High-entropy alloys. *Nat. Rev. Mater.* 4, 515–534 (2019).
5. D. Miracle, O. Senkov, A critical review of high entropy alloys and related concepts. *Acta Mater.* 122, 448–511 (2017).
6. R. Zhang et al., Short-range order and its impact on the CrCoNi medium-entropy alloy. *Nature* 581, 283–287 (2020).
7. F. Wang et al., Multiplicity of dislocation pathways in a refractory multiprincipal element alloy. *Science* 370, 95–101 (2020).
8. S. Wei et al., Natural-mixing guided design of refractory high-entropy alloys with as-cast tensile ductility. *Nat. Mater.* 19, 1175–1181 (2020).
9. X. Chen et al., Direct observation of chemical short-range order in a medium-entropy alloy. *Nature* 592, 712–716 (2021).
10. C. Chen et al., A novel ultrafine-grained high entropy alloy with excellent combination of mechanical and soft magnetic properties. *J. Magn. Magn. Mater.* 502, 166513(2020).
11. B. Zhang et al., Effects of Cu and Zn on microstructures and mechanical behavior of the medium-entropy aluminum alloy. *J. Alloys Compd.* 820, 153092 (2020).
12. J. Joseph et al., On the enhanced wear resistance of CoCrFeMnNi high entropy alloy at intermediate temperature. *Scr. Mater.* 186, 230–235 (2020).
13. Z. Pei, R. Li, M. C. Gao, G. M. Stocks, Statistics of the NiCoCr medium-entropy alloy: Novel aspects of an old puzzle. *NPJ Comput. Mater.* 6, 122 (2020).
14. Y. Wu et al., Short-range ordering and its effects on mechanical properties of high-entropy alloys. *J. Mater. Sci. Technol.* 62, 214–220 (2021).
15. B. Gludovatz et al., A fracture-resistant high-entropy alloy for cryogenic applications. *Science* 345, 1153–1158 (2014).
16. Z. Li, K. G. Pradeep, Y. Deng, D. Raabe, C. C. Tasan, Metastable high-entropy dual-phase alloys overcome the strength-ductility trade-off. *Nature* 534, 227–230 (2016).
17. J. Su, D. Raabe, Z. Li, Hierarchical microstructure design to tune the mechanical behavior of an interstitial TRIP-TWIP high-entropy alloy. *Acta Mater.* 163, 40–54 (2019).
18. Z. Wu, H. Bei, G. Pharr, E. George, Temperature dependence of the mechanical properties of equiatomic solid solution alloys with face-centered cubic crystal structures. *Acta Mater.* 81, 428–441 (2014).
19. X. Liu, Z. Pei, M. Eisenbach, Dislocation core structures and Peierls stresses of the high-entropy alloy NiCoFeCrMn and its subsystems. *Mater. Des.* 180, 107955 (2019).
20. L. Zhang, Y. Xiang, J. Han, D. J. Srolovitz, The effect of randomness on the strength of high-entropy alloys. *Acta Mater.* 166, 424–434 (2019).
21. C. Varvenne, A. Luque, W. A. Curtin, Theory of strengthening in FCC high entropy alloys. *Acta Mater.* 118, 164–176 (2016).
22. S. S. Sohn et al., Ultrastrong medium-entropy single-phase alloys designed via severe lattice distortion. *Adv. Mater.* 31, e1807142 (2019).
23. Y. Zhao, T. Nieh, Correlation between lattice distortion and friction stress in Ni-based equiatomic alloys. *Intermetallics* 86, 45–50 (2017).
24. D. Ma, M. Friák, J. von Pezold, J. Neugebauer, D. Raabe, Ab initio study of compositional trends in solid solution strengthening in metals with low Peierls stresses. *Acta Mater.* 98, 367–376 (2015).
25. Z. Pei et al., From generalized stacking fault energies to dislocation properties: Five-energy-point approach and solid solution effects in magnesium. *Phys. Rev. B Condens. Matter Mater. Phys.* 92, 064107 (2015).
26. N. L. Okamoto et al., Size effect, critical resolved shear stress, stacking fault energy, and solid solution strengthening in the CrMnFeCoNi high-entropy alloy. *Sci. Rep.* 6, 35863 (2016).
27. T. M. Smith et al., Atomic-scale characterization and modeling of 60 dislocations in a high-entropy alloy. *Acta Mater.* 110, 352–363 (2016).
28. X. Xu et al., Transmission electron microscopy characterization of dislocation structure in a face-centered cubic high-entropy alloy Al<sub>0.1</sub>CoCrFeNi. *Acta Mater.* 144, 107–115 (2018).
29. B. Joos, M. Duesbery, The Peierls stress of dislocations: An analytic formula. *Phys. Rev. Lett.* 78, 266 (1997).
30. G. Leibfried, H. D. Dietze, Versetzungsstrukturen in kubisch-flächenzentrierten kristallen. *I. Z. Phys.* 131, 113–129 (1951).
31. R. Labusch, A statistical theory of solid solution hardening. *Phys. Status Solidi* 41, 659–669 (1970).
32. D. Zhao, O. M. Løvvik, K. Marthinsen, Y. Li, Impurity effect of Mg on the generalized planar fault energy of Al. *J. Mater. Sci.* 51, 6552–6568 (2016).
33. S. Zhao, Y. Osetsky, G. M. Stocks, Y. Zhang, Local-environment dependence of stacking fault energies in concentrated solid-solution alloys. *NPJ Comput. Mater.* 5, 13 (2019).

34. Z. Pei, An overview of modeling the stacking faults in lightweight and high-entropy alloys: Theory and application. *Mater. Sci. Eng. A* 737, 132–150 (2018).
35. W. Guo et al., Shape-preserving machining produces gradient nanolaminate medium entropy alloys with high strain hardening capability. *Acta Mater.* 170, 176–186 (2019).
36. Z. Pei, B. Dutta, F. Körmann, M. Chen, Hidden effects of negative stacking fault energies in complex concentrated alloys. *Phys. Rev. Lett.* 126, 255502 (2021).
37. S. Zhao, G. M. Stocks, Y. Zhang, Stacking fault energies of face-centered cubic concentrated solid solution alloys. *Acta Mater.* 134, 334–345 (2017).
38. G. Laplanche et al., Reasons for the superior mechanical properties of medium-entropy CrCoNi compared to high-entropy CrMnFeCoNi. *Acta Mater.* 128, 292–303 (2017).
39. L. Ventelon, F. Willaime, E. Clouet, D. Rodney, Ab initio investigation of the Peierls potential of screw dislocations in bcc Fe and W. *Acta Mater.* 61, 3973–3985 (2013).
40. D. Rodney, L. Ventelon, E. Clouet, L. Pizzagalli, F. Willaime, Ab initio modeling of dislocation core properties in metals and semiconductors. *Acta Mater.* 124, 633–659 (2017).
41. V. V. Bulatov, E. Kaxiras, Semidiscrete variational Peierls framework for dislocation core properties. *Phys. Rev. Lett.* 78, 4221 (1997).
42. G. Schoeck, The Peierls model: Progress and limitations. *Mater. Sci. Eng. A* 400, 7–17 (2005).
43. S. F. Wang, A unified dislocation equation from lattice statics. *J. Phys. A Math. Theor.* 42, 025208 (2008).
44. G. Liu, X. Cheng, J. Wang, K. Chen, Y. Shen, Atomically informed nonlocal semi-discrete variational Peierls–Nabarro model for planar core dislocations. *Sci. Rep.* 7, 43785 (2017).
45. Z. Pei, G. M. Stocks, Origin of the sensitivity in modeling the glide behaviour of dislocations. *Int. J. Plast.* 106, 48–56 (2018).
46. C. Niu, C. R. LaRosa, J. Miao, M. J. Mills, M. Ghazisaeidi, Magnetically-driven phase transformation strengthening in high entropy alloys. *Nat. Commun.* 9, 1363 (2018).
47. S. Huang et al., Temperature dependent stacking fault energy of FeCrCoNiMn high entropy alloy. *Scr. Mater.* 108, 44–47 (2015).
48. J. Ding, Q. Yu, M. Asta, R. O. Ritchie, Tunable stacking fault energies by tailoring local chemical order in CrCoNi medium-entropy alloys. *Proc. Natl. Acad. Sci. U.S.A.* 115, 8919–8924 (2018).
49. W. M. Choi, Y. H. Jo, S. S. Sohn, S. Lee, B. J. Lee, Understanding the physical metallurgy of the CoCrFeMnNi high-entropy alloy: An atomistic simulation study. *NPJ Comput. Mater.* 4, 1 (2018).
50. S. Plimpton, Fast parallel algorithms for short-range molecular dynamics. *J. Comput. Phys.* 117, 1–19 (1995).
51. Y. Kamimura, K. Edagawa, S. Takeuchi, Experimental evaluation of the Peierls stresses in a variety of crystals and their relation to the crystal structure. *Acta Mater.* 61, 294–309 (2013).
52. G. Lu, N. Kioussis, V. V. Bulatov, E. Kaxiras, Generalized-stacking-fault energy surface and dislocation properties of aluminum. *Phys. Rev. B Condens. Matter Mater. Phys.* 62, 3099 (2000).
53. P. S. DeCarli, M. A. Meyers, “Design of uniaxial strain shock recovery experiments” in *Shock Waves and High-Strain-Rate Phenomena in Metals*, M. A. Meyers, L. E. Murr, Eds. (Springer, Boston, 1981), pp. 341–373.
54. M. Nord, P. E. Vullum, I. MacLaren, T. Tybell, R. Holmestad, Atomap: A new software tool for the automated analysis of atomic resolution images using two-dimensional Gaussian fitting. *Adv. Struct. Chem. Imaging* 3, 9 (2017).
55. P. Hohenberg, W. Kohn, Inhomogeneous electron gas. *Phys. Rev.* 136, B864 (1964).
56. W. Kohn, L. J. Sham, Self-consistent equations including exchange and correlation effects. *Phys. Rev.* 140, A1133 (1965).
57. G. Kresse, J. Furthmüller, Efficient iterative schemes for ab initio total-energy calculations using a plane-wave basis set. *Phys. Rev. B Condens. Matter* 54, 11169–11186 (1996).
58. J. P. Perdew, K. Burke, M. Ernzerhof, Generalized gradient approximation made simple. *Phys. Rev. Lett.* 77, 3865–3868 (1996).
59. P. E. Blöchl, Projector augmented-wave method. *Phys. Rev. B Condens. Matter* 50, 17953–17979 (1994).
60. H. J. Monkhorst, J. D. Pack, Special points for Brillouin-zone integrations. *Phys. Rev. B* 13, 5188–5192 (1976).
61. Z. Pei, M. Eisenbach, Acceleration of the particle swarm optimization for Peierls–Nabarro modeling of dislocations in conventional and high-entropy alloys. *Comput. Phys. Commun.* 215, 7–12 (2017).
62. Z. Pei, DIST: A dislocation-simulation toolkit. *Comput. Phys. Commun.* 233, 44–50 (2018).
63. Z. Pei, S. Mu, W. Ming, The local strain distribution in bilayer materials: A multiscale study. *Nanoscale* 12, 6456–6461 (2020).
64. Y. Zeng, X. Cai, M. Koslowski, Effects of the stacking fault energy fluctuations on the strengthening of alloys. *Acta Mater.* 164, 1–11 (2019).
65. A. Hunter, I. J. Beyerlein, T. C. Germann, M. Koslowski, Influence of the stacking fault energy surface on partial dislocations in FCC metals with a three-dimensional phase field dislocations dynamics model. *Phys. Rev. B Condens. Matter Mater. Phys.* 84, 144108 (2011).
66. C. Carter, S. Holmes, The stacking-fault energy of nickel. *Philos. Mag. J. Theor. Exp. Appl. Phys* 35, 1161–1172 (1977).
67. D. C. Yang, Y. H. Jo, Y. Ikeda, F. Körmann, S. S. Sohn, Effects of cryogenic temperature on tensile and impact properties in a medium-entropy VCoNi alloy. *J. Mater. Sci. Technol.* 90, 159–167 (2021).

68. D. J. Siegel, Generalized stacking fault energies, ductilities, and twinnabilities of Ni and selected Ni alloys. *Appl. Phys. Lett.* 87, 121901 (2005).
69. H. Huang et al., Critical stress for twinning nucleation in CrCoNi-based medium and high entropy alloys. *Acta Mater.* 149, 388–396 (2018).
70. Z. Zhang et al., Dislocation mechanisms and 3D twin architectures generate exceptional strength-ductility-toughness combination in CrCoNi medium-entropy alloy. *Nat. Commun.* 8, 14390 (2017).